JOURNAL OF SPACECRAFT AND ROCKETS
Vol. 32, No. 2, March–April 1995

Influence of Suboptimal Navigation Filter Design on Lunar Landing Navigation Accuracy

Dan G. Tuckness*
The University of Texas at Arlington, Arlington, Texas 76019-0018

Most onboard guidance, navigation, and control computers will be programmed using suboptimal filter design in an effort to reduce software size and computation speed. Reduction in the order of the gravity-field model of the moon is one method that can be used to reduce the number of calculations the onboard filter must perform, thus increasing the speed of computation. A result of that reduction is an increase in navigation error, which in turn directly influences the accuracy of the guidance commands. This paper investigates two prevalent lunar gravity-field models—the Ferrari 79 and the Sagitov model. A brief history of their origins and a comparison of the models are given. Particular emphasis is placed on studying their effect on guidance and navigation accuracy as the order of the onboard navigation filter model is reduced, resulting in a suboptimal filter design.

Nomenclature

A_T, A_N	= truth and navigation state gradient matrices
Alt.	= altitude, m
a	= semimajor axis, m
Cnn	= gravitational model constants
CR	= crossrange, m
DR	= downrange, m
$\boldsymbol{e}$	= eccentricity vector
G	= sensor model measurements, m
H_T, H_N	= truth and navigation observation update matrices
$\boldsymbol{h}$	= angular momentum vector, m^2/s^2
K_F	= navigation state Kalman-filter gain
$\bar{P}_T$, $\bar{P}_N$	= truth and navigation covariance matrices before navigation update
P_T, P_N	= truth and navigation covariance matrices after navigation update
Q	= unknown state noise matrix
R	= navigation measurement noise matrix
$\boldsymbol{r}$	= inertial radial vector, m
r_p	= radius of periapsis, m
v	= velocity magnitude, m/s^2
W_T, W_N	= truth and navigation weighting matrices (identity matrix for this study)
X_T, X_N	= truth and navigation state vectors, m
μ	= gravitational parameter, m^2/s^3
Φ_T, Φ_N	= truth and navigation state transition matrices
$\times$	= vector cross product

Introduction

There is no known model that completely describes the lunar gravitational field. The lack of an adequate model affects two essential navigation problems, namely, determining the position of the spacecraft at a specified time (orbit determination) and predicting the future course of the spacecraft (trajectory prediction). This, in turn, has a direct influence on the accuracy of the landing.

One of the more recent investigations into the lunar gravity field has been performed by Konopliv et al.[1] They investigate the long-term effects of a vehicle orbiting the moon. Thus, their investigation is mainly concerned with long-term navigation. "Long-term lunar navigation" refers to spacecraft position prediction that is made over intervals of more than three lunar revolutions, as for a survey spacecraft orbiting the Moon for many orbits.

Received Dec. 17, 1993; revision received Sept. 8, 1994; accepted for publication Sept. 12, 1994.

*Assistant Professor, Department of Mechanical and Aerospace Engineering, Box 19018. Member AIAA.

This paper concentrates on the deorbit and landing phase of a lunar lander and is more concerned with short-term lunar navigation, since most deorbit and landings take place within one orbit. Emphasis is placed on the development of a suboptimal navigation filter to be used onboard the lunar lander. The first Apollo mission that attempted to use an onboard suboptimal gravity model was Apollo 8. Apollo 8 used a crude triaxial lunar potential model. Apollo 10 and 11 used a 2 × 2 gravity model, and Apollo 12 used a 2 × 2 plus the $C33$ term. The Apollo missions did not include a Kalman filter, because that was not developed until late in the Apollo program. For this reason, and because that the gravity models used by the Apollo spacecraft were crude compared to modern ones, landing errors were on the order of kilometers. It is shown that even with the use of more recently derived lunar gravity models and the use of a Kalman filter, the selection of the suboptimal filter has a direct effect on the terminal landing accuracy. Two separate models are investigated in the study, in view of the differences in how they are constructed, the difference in the data the developers selected for their construction, and their reputation for being among the most accurate lunar models currently available. A brief description of each of the models is given in the next section; a more detailed description is given in Ref. 2.

The Arteimis (or Common Lunar Lander) mission is used as a reference mission for this investigation. The deorbit and landing profile is shown in Fig. 1. The Common Lunar Lander navigation accuracy requirements specify a landing target accuracy of approximately 1.5 km (1σ). A full description of the Common Lunar Lander reference mission can be found in Ref. 3. An inclination of 30 deg with a deorbit altitude of 100 km is selected for this study, based upon the work in Ref. 1.

Accuracy and History of the Various Lunar Gravity Models

The inability to mathematically model the lunar gravitational effect is often referred to as "the lunar gravity problem." Historically, two approaches were attempted to clarify the unknown gravity field. The first method used short arcs of measurements (typically 90 min) and was well adapted to detecting small gravitational irregularities on the near side of the Moon. The main drawback came from the lack of significant small arcs for the far side. Thus, the far-side gravitational field remained unresolved. The second method placed more emphasis on determining the general tendencies of the total gravity field, by estimating the low-order coefficients in the Legendre expansion. Because the data were averaged, long arcs of data (typically a month in duration) were required to provide significant tendencies. However, due to the long-arc processing, short-period harmonic information was lost. Using this method, resulted in the first estimates of the far-side gravity field of the Moon. New approaches were attempted in the late seventies to combine the advantages of these

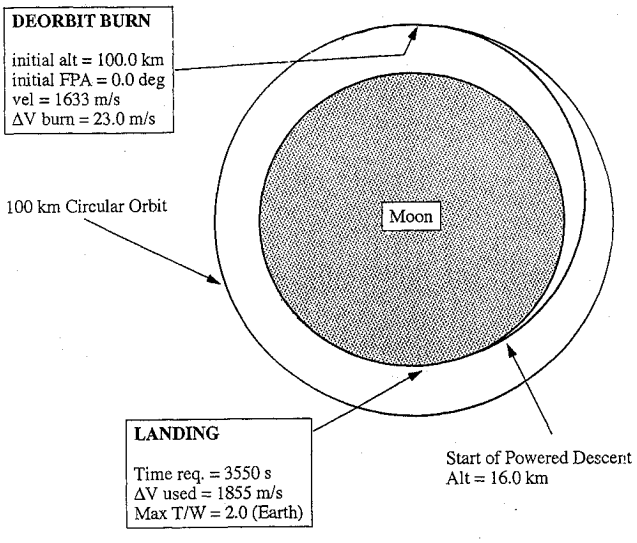

Fig. 1 CCL landing navigation scenario.

two methods, and statistical methods were introduced in an attempt to resolve the missing data of the unprobed regions. Also, during the same period, new data provided a means to update existing models.[2]

Ferrari[4–6] was one of the first to benefit from a new prolific source of lunar orbit data. Following his original method used in development of his 1977 model (F77), he attempted to provide a spherical harmonic expansion accurate up to a degree and order of 16. Ferrari's new method involved a weighted least-squares algorithm that was designed to solve a set of normal equations. He processed data from four different sources. The first set of normal equations came from his previous studies from 1975 to 1977. The second set used the analysis derived by Wong.[7] The third set came from a study performed by Ferrari and Bills in 1979[8] that aimed at determining only low-degree terms. The fourth used a set of normal equations. Details of the statistical algorithm that Ferrari used can be found in Ref. 9. Basically, the major contribution to the uncertainty in the current knowledge of the lunar gravity field is the lack of global coverage or, more specifically, the lack of any direct spacecraft measurements of the lunar gravity on the far side of the Moon and the lack of low-altitude observations near the poles.

As a consequence, the spherical harmonic coefficients must be constrained to obtain a physically meaningful global field. The a priori uncertainties for all coefficients of degree n are given by $1.5 \times 10^{-4}/n^2$. This formula is proportional to the rule that Kaula[9] developed for the Earth, but more constraining than the constant of 3.5×10^{-4} that he suggests[9] for the moon's gravity field.

Like Ferrari, Sagitov et al.[10] undertook to synthesize several previous analyses in an attempt to achieve a generalized model of the gravity field on the moon. He used a model based on the tracking of the Soviet probes (Luna 10 and 24). This model had the advantage of relatively even distribution over the lunar surface and of utilizing different inclinations of lunar orbits with respect to the lunar equator. In addition to this model, he incorporated other previously derived models, including the work of Ferrari. Sagitov also incorporated a set of data never used before. It contained four profiles of the line-of-sight accelerations of Apollo 14 through 17 subsatellities at low altitude over the central portion of the lunar surface. Konopliv et al. used two-way and three-way S-band Doppler tracking of the Lunar Orbiters I, II, III, IV, and V and Apollo 15 and 16 subsatellities. This is the most recent attempt to derive a more accurate lunar gravity model and shows close agreement with that found using Ferrari's models. Konopliv et al. were able to complete the lunar gravity field to the 60th order, an order much higher than previously derived models.

Short-Term Lunar Navigation

Short-term navigation errors result both from initial-state errors in calculating the orbit and from predicting forward to the terminal landing position with an inadequate potential model. An example of a short-term lunar navigation problem is deorbit or landing. After an inertial measurement unit (IMU) alignment, a ΔV burn of 23.0 m/s is performed to establish the deorbit trajectory. Both the deorbit and landing are perturbed by the anomalies on the gravity field. The onboard computer used for guidance and navigation probably contains only an approximation of the actual lunar gravity field. This results in trajectory errors because the lander IMU, being unable to sense gravity, uses the onboard computer model for command calculations. Because the model is inexact, error is introduced into the trajectory, which in turn maps directly into a terminal landing error. This investigation concentrates on this type of short-term navigation.

Navigation accuracy investigations based on a variety of currently available gravity-field models are important because of the differences in gravitational coefficients from model to model. Each model arrives at a different set of solutions, which are dependent on the values of the gravitational constants. Each set of solutions has a direct effect on fuel/engine sizing and other mission design constraints. Because no exact model is known, two of the better-known (and more widely used) models are incorporated in this investigation.

Effect of the Gravitational Model Coefficients

The most significant orbital variations are the long-term changes in eccentricity and argument of periapsis caused by the odd zonal terms of the gravity field. Changes in eccentricity map directly into variations in periapsis altitude. Assuming that the periapsis altitude is designed to be zero for a terminal landing (Hohman transfer), changes in the eccentricity of the orbit result in terminal landing errors. These variations have large amplitudes (hundreds of kilometers[1]) and average out over periods of hundreds of days.

Errors in the even zonal coefficients of the potential model result in secular orbital errors. These secular orbital errors are reflected in the argument of periapsis, longitude of ascending node, and mean anomaly, which all change approximately linearly with time. The even zonal coefficients also result in long-period errors in argument of periapsis and mean anomaly, and short-period errors in all the orbital elements. Short- and medium-period oscillations due to the tesseral terms are generally less significant (tens of kilometers[1]) and result in periodic errors in angular frequency. An approximate analytic solution for the long-term changes in eccentricity and argument of periapsis can be derived by assuming that the eccentricity remains small (which it must for a low-altitude orbit).

Reference 1 shows the long-term behavior for a 100-km-altitude polar orbit. This phase-space plot shows the variations in eccentricity and argument of periapsis for a number of different initial conditions. A significant feature of this plot is the existence of a frozen orbit at an eccentricity of 0.033 when the argument of periapsis is equal to 270 deg. Frozen orbits are defined as orbits with no long-term changes in eccentricity, argument of periapsis, and inclination and are represented as a single fixed point in phase space. Cook[11] gives an analytic expression for the frozen-orbit eccentricity as a function of semimajor axis, the inclination, and the zonal coefficients. Reference 1 shows the periapsis altitude uncertainty as a function of inclination for semimajor axes 100, 200, and 300 km above the surface. Using an inclination of 30 deg and an altitude of 100 km, their investigations did not result in frozen orbits. An orbit that is not frozen was desired for this investigation, so that trajectory error could accumulate and result in a worst-case scenario.

Covariance Analysis Method, Model and Initial Conditions

A covariance analysis is performed to estimate the state errors resulting from the lunar gravity-field model errors. Suboptimal extended Kalman filter designs of various orders are investigated for each gravity model in order to determine the smallest onboard navigation filter vector that would result in a nearly optimal design. The onboard navigation filter will receive observations at discrete points in time and will estimate the "cloud of uncertainty" (covariance) surrounding the state vector at these times. Its design is based on an incomplete and/or incorrect model of the actual system (truth)

Table 1 Initial covariance matrix for Common Lunar Lander (1σ)[a]

Alt., m	DR, m	CR, m	Alt. rate, m/s	DR rate, m/s	CR rate, m/s
50.000	0.0000	0.0000	0.0000	−0.9000	0.0000
0.0000	200.000	0.0000	−0.9000	0.0000	0.0000
0.0000	0.0000	50.0000	0.0000	0.0000	0.0000
0.0000	−0.9000	0.0000	0.2000	0.0000	0.0000
−0.9000	0.0000	0.0000	0.0000	0.0400	0.0000
0.0000	0.0000	0.0000	0.0000	0.0000	0.0300

[a]Reference 12: The off-diagonal terms are the cross-correlation coefficients.

dynamics. The nub of this is to assess a measure of the onboard navigation filter's suboptimal performance by means of a larger and more complex (optimal) truth model. The mathematical model and flow of the suboptimal design program used in this investigation are shown in the Appendix.

The initial covariance is based upon approximate Deep Space Network (DSN) capabilities and is given in Table 1.[12] The state elements are considered in a vehicle-centered coordinate system described as follows: (1) The DR axis is in the direction of the vehicle velocity vector, (2) the CR axis is perpendicular to the Alt. and DR directions, and (3) the Alt. axis is in the direction from the center of the lunar sphere to the vehicle.

A radar altimeter is selected for use as a secondary sensor because of its simplicity, low cost, and proven results. Using a radar altimeter allows for a better comparison of the various suboptimal filter designs than other, higher-precision secondary methods such as terrain-following navigation sensors. The higher-precision sensors remove such a large amount of the navigation error that little remains for comparison, irrespective of the suboptimal design. Therefore, in order to provide a buffer for a reasonable comparison (larger navigation error), a radar altimeter is utilized.

With the radar secondary navigation system, measurements are taken every 10 s, starting at 60-km altitude, and processed through the extended Kalman filter to aid in removing navigation uncertainty. The data used to model the radar altitude sensor error model come from Ref. 13 and consist of a 28.0-m (1σ) bias with a 4.0-m (1σ) Gaussian white-noise error. Included in the propagation of the trajectory is unknown system accelerations expressed as white noise with a standard deviation of 5.0×10^{-8} m/s^2 (1σ).

Gravity-Field Model Covariance Analysis

The first investigation consists in determining the navigation accuracy capabilities of the suboptimal filter design in removing the navigation uncertainties. Table 2 gives the various cases (filter sizes) for the investigation. Figures 2–5 depict the covariance of the position and velocity channels as a function of time for a near-side deorbit burn that results in a far-side landing when using the full 16×16 navigation filter.

Two trajectories are investigated. The first trajectory (far-side landing) assumes the IMU is aligned and the initial covariance from the DSN (Table 1) is transmitted to the spacecraft just prior to the deorbit burn on the near side of the moon. Because the deorbit burn is on the near side, a far-side landing results. The second trajectory (near-side landing) assumes the IMU is aligned and the initial covariance from the DSN (Table 1) is transmitted to the spacecraft when the spacecraft is on the near side. However, the deorbit burn takes place on the far side of the moon, resulting in a near-side landing.

Navigation Error

The differences between a full 16×16 lunar gravity model and the suboptimal filter models are calculated using the following relations: $(\Delta\text{filter [channel] error})^2 = (16 \times 16\text{ [channel] error})^2 - (\text{suboptimal filter [channel] error})^2$, where the various channels are Alt., DR, CR, Alt. Vel., DR Vel., and CR Vel.

Tables 3 and 4 depict the performance of the suboptimal filters for the near-side and far-side landings. As observed in the two tables, there is a slight difference in the suboptimal filters between the Ferrari 79 and Sagitov gravity fields. Also, the fourth-order zonal-harmonic suboptimal filter offers nearly the same performance as

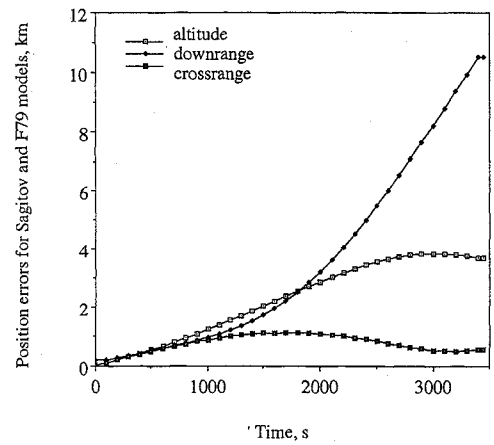

Fig. 2 Positional covariance values (1σ), using the Sagitov and F79 gravity models, vs time.

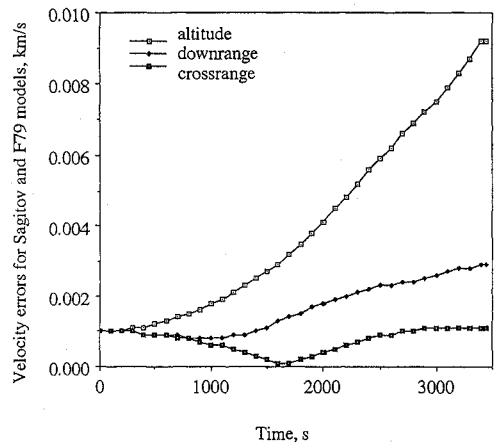

Fig. 3 Velocity covariance values (1σ), using the Sagitov and F79 gravity models, vs time.

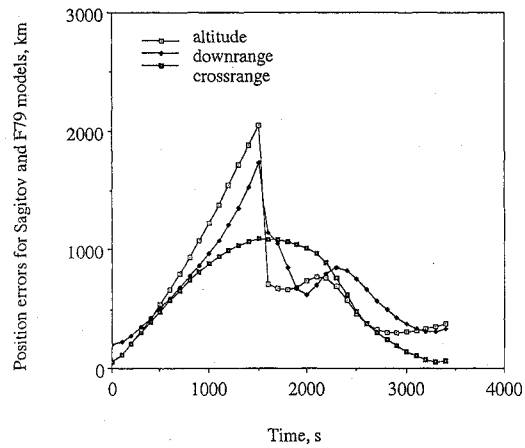

Fig. 4 Positional covariance values (1σ), using the Sagitov or F79 gravity model with updates, vs time.

the 6×6 model at a much lower filter size cost. The 6×6 filter requires a 51-parameter state vector, whereas the fourth-order zonal filter requires a 9-parameter state vector.

All model sizes for both gravity models meet the "loose" mission accuracy requirements of 1.5-km landing accuracy. Therefore, for navigation purposes only, mission terminal landing accuracies can be met using suboptimal filters using only the inverse square law. However, in missions that require high-precision landings, that is, landing accuracies on the order of tens of meters, only the higher-order suboptimal filter models offer the necessary accuracy.

The near-side landing results in a larger covariance (greater navigation uncertainty) because the spacecraft travels from the near side

Table 2 Various navigation cases investigated

Ferrari 79 gravity model: truth model uses the full 16 × 16 model

Far-side landing:

Case 1: Navigation filter uses the first 6 × 6 elements of the full model.
Case 2: Navigation filter uses J_2–J_{16} zonal harmonics only.
Case 3: Navigation filter uses J_2–J_4 zonal harmonics only.
Case 4: Navigation filter uses J_2 only.
Case 5: Navigation filter uses inverse-square law only.

Near-side landing:

Case 6: Navigation filter uses the first 6 × 6 elements of the full model.
Case 7: Navigation filter uses J_2–J_{16} zonal harmonics only.
Case 8: Navigation filter uses J_2–J_4 zonal harmonics only.
Case 9: Navigation filter uses J_2 only.
Case 10: Navigation filter uses inverse-square law only.

Sagitov gravity model: truth model uses the full 16 × 16 model

Far-side landing:

Case 11: Navigation filter uses the first 6 × 6 elements of the full model.
Case 12: Navigation filter uses J_2–J_{16} zonal harmonics only.
Case 13: Navigation filter uses J_2–J_4 zonal harmonics only.
Case 14: Navigation filter uses J_2 only.
Case 15: Navigation filter uses inverse-square law only.

Near-side landing:

Case 16: Navigation filter uses the first 6 × 6 elements of the full model.
Case 17: Navigation filter uses J_2–J_{16} zonal harmonics only.
Case 18: Navigation filter uses J_2–J_4 zonal harmonics only.
Case 19: Navigation filter uses J_2 only.
Case 20: Navigation filter uses inverse-square law only.

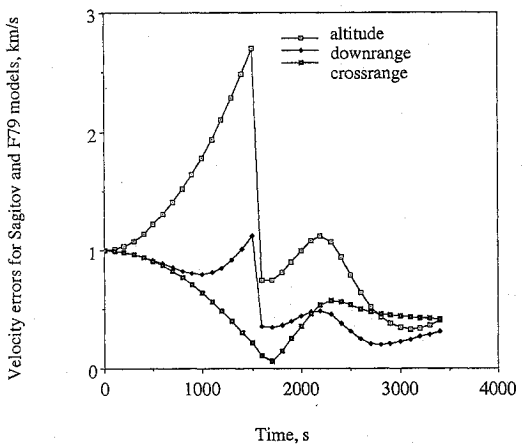

Fig. 5 Velocity covariance values (1σ), using the Sagitov or F79 gravity model with updates, vs time.

(where the IMU is aligned and the covariance is initialized) to the far side (where the deorbit burn takes place) and then back around the near side for touchdown, resulting in a navigation duration twice as long as the farside landing. Because the near-side landing takes approximately twice as long as the far-side and the covariance increases with time, the near-side landing results in greater errors.

A problem arises with the near-side landing because the spacecraft must perform the deorbit burn on the far side, where transmissions from the Earth are blocked by the moon. The IMU can still perform an alignment on the farside. However, the high-precision DSN processed covariance cannot be transmitted up to the spacecraft. Therefore, the covariance the spacecraft uses for the far-side deorbit burn is the covariance that results from propagating the initial covariance (transmitted to the spacecraft on the near side) to the far-side deorbit burn position. Table 5 shows the values of the variance obtained for the deorbit burn position on the far side using the two separate gravity models. Note: both gravity models resulted in approximately the same error values (within 1 m of one another) for both the aided and the unaided navigation scenario.

Table 6 shows the 1σ difference values of the position and velocity errors on the dark side during the deorbit burn. These 1σ values are the RSS difference between the 16 × 16 truth model covariance

Table 3 Navigation accuracy differences of far-side landings

Case	Alt., m	DR, m	CR, m	Alt. Vel., m/s	DR Vel., m/s	CR Vel., m/s
			Ferrari 79			
1	0.00	3.88	2.12	0.00	0.00	0.00
2	3.67	5.49	3.16	0.01	0.00	0.01
3	0.00	3.88	2.21	0.00	0.00	0.00
4	2.59	5.49	2.35	0.01	0.00	0.01
5	6.35	10.28	3.49	0.01	0.01	0.01
			Sagitov			
11	0.00	2.75	1.86	0.00	0.00	0.00
12	3.67	6.14	2.58	0.01	0.00	0.01
13	0.00	2.75	1.79	0.00	0.00	0.00
14	3.67	6.14	1.86	0.01	0.00	0.01
15	6.35	10.98	2.77	0.01	0.01	0.01

Table 4 Navigation accuracy differences of near-side landings

Case	Alt., m	DR, m	CR, m	Alt. Vel., m/s	DR Vel., m/s	CR Vel., m/s
			Ferrari 79			
6	12.0	14.7	37.4	0.01	0.03	0.04
7	44.7	66.9	191.0	1.51	0.84	0.74
8	12.2	8.2	35.1	0.02	0.02	0.04
9	3.4	70.8	33.2	0.04	0.06	0.04
10	15.5	157.7	42.1	0.11	0.11	0.04
			Sagitov			
16	6.8	16.4	16.6	0.02	0.00	0.01
17	54.4	64.2	165.7	1.42	0.72	1.07
18	7.6	26.7	14.6	0.04	0.01	0.01
19	6.3	43.3	11.8	0.03	0.03	0.01
20	21.3	131.7	20.7	0.10	0.08	0.01

Table 5 Navigation error for far-side deorbit burn and near-side landing

	Alt., m	DR, m	CR, m	Alt. Vel., m/s	DR Vel., m/s	CR Vel., m/s
			Deorbit burn			
Sagitov	4,037.4	11,232.0	501.9	9.5	3.0	1.0
Ferrari 79	4,034.4	11,222.0	501.8	9.5	2.9	0.1
			Landing (unaided)			
Sagitov	503.9	22,757.0	1060.2	19.4	15.1	14.9
Ferrari 79	483.2	22,610.0	1073.7	19.3	15.3	14.5
			Landing (aided)			
Sagitov	71.7	286.0	78.6	0.5	0.1	0.9
Ferrari 79	71.7	286.0	80.1	0.5	0.1	0.9

Table 6 State covariance differences between the full truth model (16 × 16) and the suboptimal filter models during the farside deorbit burn

Case	Alt., m	DR, m	CR, m	Alt. Vel., m/s	DR Vel., m/s	CR Vel., m/s
			Ferrari 79			
6	63.7	63.6	357.3	0.03	0.32	0.17
7	63.6	102.5	145.8	1.05	0.49	0.22
8	65.6	56.8	357.3	0.04	0.28	0.16
9	68.5	130.3	206.2	0.04	0.46	0.19
10	82.0	190.7	291.6	0.05	0.66	0.22
			Sagitov			
16	57.5	123.9	145.9	0.06	0.41	0.24
17	79.0	127.1	461.2	0.07	0.60	1.29
18	60.3	139.3	206.3	0.06	0.41	0.24
19	62.7	56.9	357.3	0.06	0.56	0.26
20	77.18	123.9	505.2	0.07	0.73	0.29

Table 7 Absolute trajectory guidance error resulting from the navigational differences between the full truth model (16 × 16) and the suboptimal filter models during the far side deorbit burn

	Error at periapsis, m					
Error at ΔV burn[a]	ΔAlt.	ΔDR	ΔCR	ΔAlt. Vel.	ΔDR Vel.	ΔCR Vel.
Alt. (±82)	228	12	Neg.	2	3068	0.11
DR (±191)	Neg.	6457	Neg.	2624	Neg.	Neg.
CR (±505)	Neg.	Neg.	477	Neg.	Neg.	Neg.

[a]Neg. = negligible.

and the suboptimal filter model error and thus depict the suboptimal filter state covariance error during the deorbit burn.

Guidance Error

The uncertainty in the state vector directly relates to the uncertainty in the magnitude of the deorbit-burn state vector, in the deorbit-burn direction (flight-path angle), and in the deorbit-burn magnitude. The uncertainty in the magnitude of the deorbit burn does not pose a problem with the near-side deorbit burn, because the covariance is updated just prior to the deorbit burn for a far-side landing. This uncertainty in the deorbit burn on the far side gives a control (or guidance) type of deorbit error, resulting in a controller-induced terminal landing error in addition to the landing navigation error. Because the IMU is aligned using a star tracker prior to the deorbit burn, the attitude error should be very small. Therefore, neglecting attitude uncertainty, the resulting landing control error is a function of the uncertainty in the position and velocity of the lander during the deorbit burn. Using the basic unperturbed two-body orbital relation

$$\frac{d\boldsymbol{r}}{dt} \times \boldsymbol{h} = \frac{\mu}{r}(\boldsymbol{r} + r\boldsymbol{e}) \tag{1}$$

we have

$$\bar{e} = \frac{\bar{v} \times \bar{h}}{\mu} - \frac{\bar{r}}{r} \tag{2}$$

and

$$\frac{v^2}{2} - \frac{\mu}{r} = -\frac{\mu}{2a} \tag{3}$$

$$r_p = a(1 - e) \tag{4}$$

$$\boldsymbol{h} = \boldsymbol{r} \times \boldsymbol{v} \tag{5}$$

The following relationships can be constructed to relate the state parameters during the deorbit burn to a radius of periapsis error (landing error):

$$\Delta \boldsymbol{R}_{1p} = \frac{(1 - |\boldsymbol{e}|)\boldsymbol{e}\mu r}{(2\mu - r|\boldsymbol{v}|^2)\boldsymbol{e}} - \boldsymbol{r}_0 \tag{6}$$

$$\Delta \boldsymbol{R}_{2p} = r_p \frac{\boldsymbol{e}}{|\boldsymbol{e}|} \tag{7}$$

where

$$\boldsymbol{r}_0 = \begin{bmatrix} R_{\text{moon}} \\ 0 \\ 0 \end{bmatrix}$$

It must be noted that these relations do not include the perturbing effects of the geopotential model but offer a close approximation in analytical form that can be used to gain insight to the current problem. Equation (6) is the general equation for finding the error in the radius of periapsis direction resulting from the deorbit-burn error. The relation breaks down when finding the error in the altitude channel if the initial dispersion is in the altitude position or downrange velocity directions. However, $\Delta \boldsymbol{R}_{2p}$ is an alternate equation that can be used to find the resulting radius of periapsis when the dispersions are a function of the altitude position or downrange velocity directions.

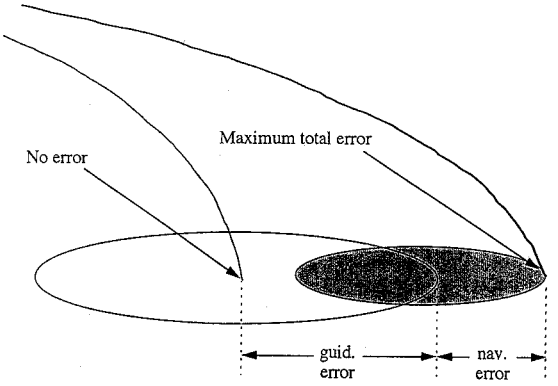

Fig. 6 Navigation and guidance errors contributing to the total landing error.

Using Eqs. (6) and (7) above and the differences between the full truth model (16 × 16) and the suboptimal filter models found in Table 6, the terminal landing errors resulting from guidance errors (or errors in the navigation states during guidance deorbit burn commands) can be found. Table 7 shows the resulting absolute error as a function of the maximum deorbit state errors in the Alt., DR, CR, Alt. Vel., DR Vel., and CR Vel. channels found in Table 6. Note that "neg." in Table 7 stands for negligible, meaning errors less than 0.1 m. Also, velocity landing errors are not depicted, because the tolerable errors in landing velocity are a function of the structural robustness of the lander and the amount of fuel (ΔV) allocated for the terminal braking maneuver. Also, most missions carry a terminal Doppler radar to measure velocities when the lander is close to the surface. It is used to remove most of the terminal landing error.

Notice that error in the downrange channel during the deorbit burn results in the largest error upon periapsis arrival. This periapsis arrival error could also be taken as resulting from an error in the timing of the deorbit burn. The two next largest errors (altitude and velocity errors during the deorbit burn) are related through the uncertainty in the flight-path angle. Therefore, the main contributions to landing guidance error are the uncertainty in the deorbit-burn timing and in the flight-path angle during the deorbit burn. These two errors are larger than the 1.5-km landing-error limit required of the navigation system.

An approximation for the maximum landing error can be found by finding the root sum squared (RSS) values of the guidance and navigation errors combined. In essence, this effort requires the summing the major axes of the navigation and guidance error ellipsoids. Figure 6 gives a graphical description of a two-dimensional example (assuming the altitude error is neglected) in finding the maximum error ellipse. The two examples show the maximum total DR landing-error difference between the 16 × 16 gravity model and two other models (case 6, the inverse-square suboptimal model; case 10, the 6 × 6 suboptimal model) when the navigation and guidance errors are combined. Let the difference between the landing errors using the 16 × 16 and the inverse-square gravity models be denoted by Δ_{LE}, and the terminal guidance error, resulting from the difference between the deorbit-navigation-burn errors using the 16 × 16 and inverse-square gravity models, be denoted by Δ_{GE}. Using this notation and the following equation, the RSS total maximum DR landing error can be found:

$$(\text{RSS total maximum DR landing error})^2 = (\Delta_{\text{LE}})^2 + (\Delta_{\text{GE}})^2$$

for case 6 this results in

$$\text{RSS total DR error} = (157.7^2 + 6458^2)^{0.5} = 6459.9 \text{ m}$$

and for case 10

$$\text{RSS total DR error} = (14.7^2 + 2150.7^2)^{0.5} = 2150.8 \text{ m}$$

The approximations used in the two examples include the facts that the guidance error is based on a nonperturbed landing trajectory and that the navigation error is a 1σ landing error. Although not exact, both assumptions are fairly close to those in more robust models and should offer a meaningful initial investigation. Upon consideration of the two example problems, it is found that updating the covariance as close to the far-side deorbit burn as possible reduces the guidance error introduced into the deorbit burn. Therefore, that should be an important goal in the design phase of the mission and is a topic for future investigations.

Conclusions

This paper investigates how suboptimal navigational models, used to describe the lunar gravity field, affect terminal landing accuracy. Emphasis is placed on the development of a suboptimal navigation filter, and it is shown that suboptimal filter design has a direct effect on the terminal landing accuracy. The Arteimis (or Common Lunar Lander) mission, with a landing target accuracy requirement of approximately 1.5 km (1σ), is used as a reference mission for this investigation. Under the constraints of a 1.5-km landing error, the navigation error is determined not to be a major accuracy problem for either the far-side landing or the near-side landing.

However, for a near-side landing, the ΔV burn must be executed on the far side. Because the state covariance cannot be updated on the far side prior to the deorbit burn, the accumulated errors in the state directly affect the accuracy of the calculated flight-path angle and the timing of the deorbit burn. Inaccuracy of the calculated flight-path angle and the timing of the deorbit burn result in a guidance (or control) error, which in turn produces a landing state error. It is found that the guidance/control error can easily violate the 1.5-km landing accuracy requirement. Thus, it is essential that the covariance be updated as close to the deorbit burn as possible in order to reduce the guidance error during the deorbit burn. Note that the last covariance update prior to the far-side burn is 180 deg away from the deorbit-burn point. Though it may be possible to supply the lander with an updated covariance just prior to occultation with respect to the Earth, an investigation into updating the covariance 180 deg away from the deorbit burn point is necessary in order to investigate a worst-case scenario.

Another approach to resolving the landing error (usually with a higher cost) is to use a more accurate secondary navigation system to augment (or replace) the radar altimeter. Basically, the radar altimeter measurements did not improve relative navigational knowledge in the crossrange directions, because very little, if any, maneuvering is performed in the crossrange plane, so that the crossrange navigation channel is nearly unobservable. This results in a small value for the Kalman gain for the crossrange channel. Because there is no atmosphere, there is no common aerodynamic force shared between the altitude descent rate and the downrange velocity (coupling term). Thus, altitude updates provide no downrange or flight-path angle information. However, the velocity magnitude is updated indirectly from altitude measurements and can be used to back out flight-path angle information, because of the high correlation between altitude and velocity errors resulting from orbital energy knowledge.

Appendix: Mathematical Model and Flow of the Suboptimal Design Program

1) Compute the gradient matrix of the truth equations of motion with respect to the state variables using a central-difference scheme:

$$A_T(t) = \frac{\partial F(X_T, t)}{\partial X_T} \tag{A1}$$

2) Compute the time derivative of the truth state transition matrix:

$$\dot{X}_T = f(X_T, t) \tag{A2}$$

$$\dot{\Phi}_T = A_T \Phi_T \tag{A3}$$

3) Integrate the truth state vector and the truth state transition matrix from time t_n to time t_{n+1} using a fourth-order, fixed-step-size Runge–Kutta integrator:

$$X_T = \int \dot{X}_T \, dt \tag{A4}$$

$$\Phi_T = \int \dot{\Phi}_T \, dt \tag{A5}$$

4) Propagate the truth-side covariance matrix and state vector:

$$P_T = \Phi_T \bar{P}_T \Phi_T^T + Q \tag{A6}$$

5) Compute the partial derivatives of the navigation equations of motion with respect to the state variables, using a central-difference scheme:

$$A_N(t) = \frac{\partial F(X_N, t)}{\partial X_N} \tag{A7}$$

6) Compute the time derivative of the navigation state transition matrix:

$$\dot{X}_N = f(X_N, t) \tag{A8}$$

$$\dot{\Phi}_N = A_N \Phi_N \tag{A9}$$

7) Integrate the navigation state vector and the "navigation" state transition matrix from time "t_n" to time t_{n+1}, using a fourth-order, fixed-step-size Runge–Kutta integrator:

$$X_N = \int \dot{X}_N \, dt \tag{A10}$$

$$\Phi_N = \int \dot{\Phi}_N \, dt \tag{A11}$$

8) Propagate the navigation-side covariance matrix and state vector:

$$P_N = \Phi_N \bar{P}_N \Phi_N^T + Q \tag{A12}$$

9) Compute the truth observation update matrix:

$$H_T = \frac{\partial G(X_T, t)}{\partial X_T} \tag{A13}$$

10) Compute the navigation observation update matrix:

$$H_N = \frac{\partial G(X_N, t)}{\partial X_N} \tag{A14}$$

11) Compute the Kalman-filter gain, using the navigation observation update matrix:

$$K_N = \bar{P}_N H_N^T \left(H_N \bar{P}_N H_N^T + R\right)^{-1} \tag{A15}$$

12) Update the truth covariance matrix using the navigation-derived Kalman filter gain:

$$P_T = (I - W_T K_N H_T) \bar{P}_T (I - W_T K_N H_T)^T + W_T K_N R K_N^T \tag{A16}$$

13) Update the "navigation" covariance matrix using the navigation Kalman filter gain:

$$P_N = (I - W_N K_N H_N) \bar{P}_N (I - W_N K_N H_N)^T + W_N K_N R K_N^T \tag{A17}$$

14) Set $\bar{P}_T = P_T$ and $\bar{P}_N = P_N$ for next iteration.

15) Recondition the covariance matrices to keep them positive definite.

16) Print results.

17) Go back to Step 1 for the next step in the integration.

Acknowledgment

The author thanks the State of Texas, which supported this research under the Advanced Technology Program, Grant 003656089.

References

[1]Konopliv, A. S., Sjogren, W. L., Wimberly, R. N., Cook, R. A., and Vijayaraghavan, A., "A High Resolution Lunar Gravity Field and Predicted Orbit Behavior," American Astronomical Society, Paper 93-622, Aug. 1993.

[2]Tuckness, D. G., and Jost, B., "A Critical Analysis of the Lunar Gravity Potential Model," *Applied Mathematics and Computation* (submitted for publication).

[3]Tuckness, D. G., "Selenopotential Field Effects on Lunar Landing Accuracy," *Journal of Spacecraft and Rockets*, Vol. 32, No. 2, pp. 370–374.

[4]Ferrari, A., "Lunar Gravity, the First Farside Map," *Science*, Vol. 188, No. 4195, June 1975, pp. 1297–1300.

[5]Ferrari, A., "Lunar Gravity, a Harmonic Analysis," *Journal of Geophysical Research*, Vol. 82, No. 20, 1977, pp. 3065–3084.

[6]Ferrari, A., and Ananda, M., "Lunar Gravity, Long-Term Keplerian Rate Method," *Journal of Geophysical Research*, Vol. 82, No. 20, July 1977, pp. 3085–3097.

[7]Wong, L., Buechler, G., and Doens, W., "A Surface-Layer Representation of the Lunar Gravity Field," *Journal of Geophysical Research*, Vol. 76, No. 26, Sept. 1971, pp. 6220–6236.

[8]Ferrari, A., and Bills, B., "A Harmonic Analysis of Lunar Gravity," *Journal of Geophysical Research*, Vol. 85, No. B2, 1980, pp. 1013–1025

[9]Kaula, W. M., "The Investigation of the Gravitational Fields of the Moon and Planets with Artificial Satellites," *Advanced Space Science Technology*, Vol. 5, 1963, pp. 210–230.

[10]Sagitov, M. U., Bodri, B., Nazarenko, V. S., and Tadzhodinoz, Kh. G., *Lunar Gravimetry*, 1st ed., Academic Press, New York, 1986.

[11]Cook, R. A., "Long-Term Behavior of Near-Circular Orbits in a Zonal Gravity Field," American Astronomical Society, Paper 91-463, Aug. 1990.

[12]Tuckness, D. G., "Future Lunar Landing Navigation Schemes with Emphasis on Precision Landings," *Journal of the Institute of Navigation*, Vol. 41, No. 2, 1994, pp. 215–228.

[13]Gamble, J. D., et al., "JSC Pre-phase A Study, Mars Rover Sample Return Mission, Aerocapture, Entry, and Landing Element," NASA Report JSC-23230, May 1989.

H. R. Anderson
Associate Editor